Photoacoustics 31 (2023) 100481

Contents lists available at ScienceDirect

Photoacoustics

journal homepage: www.elsevier.com/locate/pacs

Research article

Imaging phonon eigenstates and elucidating the energy storage characteristics of a honeycomb-lattice phononic crystal cavity

P.H. Otsuka [a,*], R. Chinbe [a], M. Tomoda [a], O. Matsuda [a], Y. Tanaka [a], D.M. Profunser [a], S. Kim [b], H. Jeon [b], I.A. Veres [c], A.A. Maznev [d], O.B. Wright [e,f]

[a] Division of Applied Physics, Faculty of Engineering, Hokkaido University, Sapporo 060-8628, Japan
[b] Department of Physics and Astronomy, Seoul National University, Seoul 08826, Republic of Korea
[c] Research Center for Non-Destructive Testing GmbH, Altenberger Str. 69, Linz 4040, Austria
[d] Department of Chemistry, Massachusetts Institute of Technology, Cambridge 02139, United States of America
[e] Graduate School of Engineering, Osaka University, Yamadaoka 2-1, Suita, Osaka 565-0871, Japan
[f] Hokkaido University, Sapporo 060-0808, Japan

ARTICLE INFO

Keywords:
Phononics
Cavity
Imaging
Phononic crystal
Ultrasonics
Picosecond
Optical
Damping
Q factor

ABSTRACT

We extend gigahertz time-domain imaging to a wideband investigation of the eigenstates of a phononic crystal cavity. Using omnidirectionally excited phonon wave vectors, we implement an ultrafast technique to experimentally probe the two-dimensional acoustic field inside and outside a hexagonal cavity in a honeycomb-lattice phononic crystal formed in a microscopic crystalline silicon slab, thereby revealing the confinement and mode volumes of phonon eigenstates—some of which are clearly hexapole in character—lying both inside and outside the phononic-crystal band gap. This allows us to obtain a quantitative measure of the spatial acoustic energy storage characteristics of a phononic crystal cavity. We also introduce a numerical approach involving toneburst excitation and the monitoring of the acoustic energy decay together with the integral of the Poynting vector to calculate the Q factor of the principal in-gap eigenmode, showing it to be limited by ultrasonic attenuation rather than by phonon leakage to the surrounding region.

1. Introduction

Cavities in phononic crystals (PCs) are structures formed by defects in the material's periodicity. These can result in cavity modes at frequencies inside a phononic band gap, so that acoustic energy is localized in the vicinity of the defect. Such cavities have proved useful in confining acoustic energy down to sub-micron scales, because of their versatility and tailorable frequency response [1–17], while also having the potential for high Q factors [6,9,11,15,17–20].

Recent studies of cavities in PCs have demonstrated various applications, for example in sensing fluid-mixture ratios based on shifts in cavity resonance [13], in acoustic filtering based on coupling between a waveguide and a point defect [21], and in directional control of acoustic radiation patterns [22]. Potential future applications for PC cavities in which both the Q factor as well as spatial localization could be particularly important include energy harvesting [7,14,23] and timing in radio-frequency circuits as a low power alternative to crystal oscillators [24].

In the electromagnetic case, spatial confinement in photonic crystals is important for determining the strength of optical-matter interactions, such as in the Purcell effect—the enhancement of the rate of spontaneous atomic emission [25]. Studies of photon confinement in planar triangular-lattice photonic crystal cavities have revealed in-gap hexapole modes and their energy density distribution [26–28]. Although less frequently reported than for the separate cases of photonic or phononic crystals, spatial confinement in systems combining these two types of structure also have important applications, for example, in localized opto-mechanical interactions [29–33].

Both spatial localization and spectral purity of modes in acoustics are limited by the design of the structure. Slabs often perform better than bulk materials, where acoustic energy in the latter case can be lost to the body of the material. Cavities in slabs therefore generally have the advantage of a higher Q factor and lower mode volumes than in bulk materials [6,12,13,20,34–41].

To study spatial confinement of surface or plate waves in phononics one ideally needs experimental access to the full 2D (two-dimensional) lateral acoustic field distribution. Cavity modes in a square-lattice PC with mercury-filled holes in an aluminium slab were imaged by Torres et al., showing acoustic confinement in the PC band gap at ~1 MHz [1]. Cavity modes in a honeycomb-lattice PC silicon slab possessing a wide

* Corresponding author.
E-mail address: paul@eng.hokudai.ac.jp (P.H. Otsuka).

https://doi.org/10.1016/j.pacs.2023.100481
Received 7 February 2023; Received in revised form 23 March 2023; Accepted 23 March 2023
Available online 11 April 2023

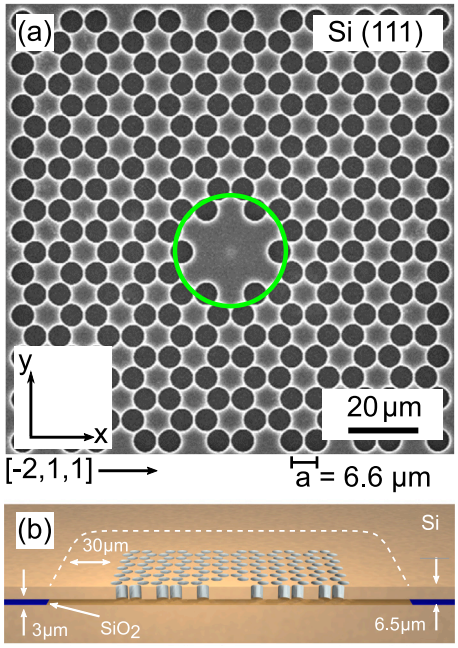

Fig. 1. Sample geometry. (a) SEM image. The Si [−2,1,1] crystal axis lies in the x direction. The green circle of radius r_0 = 15 µm is taken to define the cavity in the analysis. (b) Sample cross section taken through the centre of the cavity. The Si slab is supported by an SiO_2 layer on a (111) Si substrate. The SiO_2 (blue) region directly below the PC region was etched away, leaving a free-standing slab extending 30 µm beyond the outside boundary of the PC region. The white dashed line indicates the border of this free-standing region.

band gap [35] were imaged in 1D at ~25 MHz by Marchel et al. [12]. Similarly, cavity modes in a snowflake-hole triangular lattice PC slab of GaAs at ~0.5 GHz were imaged by Hatanaka and Yamaguchi [20]. However, in all these studies no systematic investigation over a wide range of frequencies was carried out, nor was the spatial decay of the acoustic field in the PC cavity 'walls' elucidated, which determines the volume for energy storage.

Studying PC cavity modes by imaging at GHz frequencies is of broad interest, notably in sensing and telecommunications; at such frequencies, time-resolved methods are effective in revealing acoustic eigenmode field patterns in real space and **k**-space [42–46]. Here we use a time-resolved optical pump-probe technique to image the 2D acoustic field in a microscopic PC-slab cavity in the range ~0.1–1 GHz. By comparison with numerical simulations, we investigate the frequency response and mode field pattern both inside and outside the cavity, thereby probing the modal spatial localization, the mode volume and the acoustic energy storage profiles. We also simulate the Q factor for the main eigenmode inside the forbidden gap, i.e., the one with the highest Q factor, by a time-domain approach, and elucidate the role of ultrasonic attenuation.

2. Methods

2.1. Sample geometry

The sample consists of a microscopic honeycomb lattice of circular holes in a (111) silicon-on-insulator wafer produced by a dry etching process [47]. Figure 1(a) shows a scanning-electron-microscope (SEM) image of the sample surface, whereas Fig. 1(b) shows the layer structure. An approximately hexagonal cavity is formed by the absence of 6 holes in the sample centre. The 2D phononic crystal lattice provides in-plane acoustic confinement whereas the slab surfaces provide out-of-plane confinement. The insulator (silicon oxide) was removed by etching to leave a free-standing crystalline Si slab of thickness 6.5 µm extending 30 µm beyond the edge of the PC region, which occupies 120 × 120 µm^2. The diameter of the through-holes is 5.8 µm (estimated from SEM images), and the hole spacing is a = 6.6 µm (lattice vector length $\sqrt{3}a$ and filling factor 0.53). The hole pattern has 6-fold symmetry, but the (111) face of the Si substrate has 3-fold crystalline symmetry, with the crystal axes aligned along the symmetry directions of the hole array [see Fig. 1(a)]. Phonon dispersion simulations (see Section 3.2) reveal a complete (i.e., omnidirectional) band gap between 230 and 320 MHz, characteristic of phononic honeycomb lattices in thin plates [48,49]. Our design provides a sufficient number of unit cells around the cavity for the PC to confine phonons at bandgap frequencies. A Pt dot of diameter 2.5 µm and thickness 30 nm is deposited in the cavity centre by focused ion beam (FIB) deposition to facilitate optoacoustic excitation.

2.2. Experimental method

Laterally propagating phonons in the slab are excited and detected using an optical pump-probe set-up with a Ti:sapphire femtosecond laser of repetition rate f_{rep} = 80.4 MHz, generating pulses of duration ~100 fs that are focused with a 50× objective lens onto the sample. The pump beam, of wavelength of 415 nm (obtained with a second-harmonic crystal) and a FWHM (full-width-at-half-maximum) spot diameter of ~1 µm, excites a broadband surface-phonon wavepacket at the Pt dot in the centre of the PC cavity with a pulse energy of ~0.3 nJ by thermoelastic expansion. The probe beam, of wavelength 830 nm and FWHM spot diameter ~2 µm, passes through a variable delay relative to the pump beam, and after normal-incidence reflection from the sample passes through a common-path interferometer system that detects the out-of-plane (z-directed) surface particle velocity [50] over the 12.4 ns laser repetition period at 0.43 ns intervals with a pulse energy of ~0.1 nJ. The pump beam is chopped at 1 MHz for lock-in detection purposes. While keeping the pump spot fixed, the probe spot is scanned across the sample to generate images of the 2D acoustic wave field evolution over an area of ~120 × 120 µm^2 in the x–y plane, allowing animations of the surface motion to be obtained at acoustic frequencies up to ~1 GHz. The approach is similar to that used for previous PC imaging studies, making use in our case of two probe pulses at an interval of 300 ps to monitor the out-of-plane surface particle velocity [43–45]. The use of two probe pulses allows a differential measurement, resulting in the imaging of the out-of-plane velocity rather than the displacement. The continuous repetition of the pump laser pulses induces a nondestructive local steady-state heating of ~10 K (i.e., the temperature rise at the centre of the pump spot that would occur if the pump beam had a constant intensity with the same average power) and a transient rise of ~1000 K [46,51].

3. Results

3.1. Experimental results

Figure 2(a) and (b) show experimental snapshots of the out-of-plane acoustic particle velocity (u_z) field at two different delay times 6.8 and 8.1 ns (after the arrival of an optical pump pulse), superimposed on the static probe-beam reflectance field $R(x, y)$ [see Fig. 2(e)] to clearly reveal the hole positions and illustrate the out-of-plane motion. Images without an R contribution are shown in Fig. 2(c), (d). The 6-fold symmetry of the PC structure and concentration of acoustic amplitude in the central cavity region are evident. This confinement is maintained over the whole time window of measurement (see the Supplementary Information for a time-domain 2D animation of 29 frames). The sampled temporal variation obtained from the sum of three symmetrically equivalent points in the cavity is shown in Fig. 2(f), dominated by a 402 MHz oscillation. (Use of three points allows a better signal-to-noise ratio to be obtained.) Periodic laser pulse excitation implies that acoustic generation occurs at integral multiples ($f = mf_{rep}$)

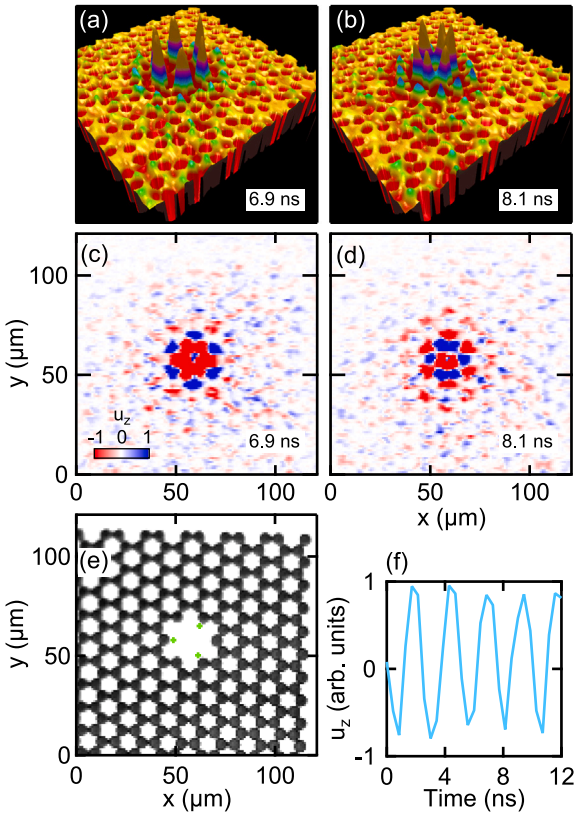

Fig. 2. Time-domain experimental images and data for the honeycomb PC cavity sample. (a)–(d) Experimental time-resolved images of the acoustic field at 6.9 and at 8.1 ns. (a), (b) 3D renderings made by combining out-of-plane surface velocity (u_z) and reflected probe intensity fields. (c), (d) Images of the out-of-plane surface particle velocity u_z. (e) Experimental image of the probe beam reflectivity R. (f) Time-domain variation of u_z sampled at three symmetrically equivalent points in the cavity, as shown in (e) in green. The colour scales are the same for (a), (b) and for (c), (d).

of the laser repetition rate. The proximity of 402 MHz (m = 5) to a cavity resonance leads to this oscillation dominating the time-domain response. Although this mode is outside the band gap, there is still a confinement effect owing to the close proximity of the holes.

To elucidate the frequency dependence of the acoustic eigenstate distribution we perform temporal Fourier transforms of the u_z data, taking the real part. Figure 3(a) (left-hand column) shows frequency-resolved acoustic fields thus obtained at six equally spaced frequencies determined by f_{rep} = 80.4 MHz. (Modulus and phase plots are given together with data up to ~1 GHz in the Supplementary Information.) Figure 3(b) shows the corresponding frequency-resolved acoustic fields in **k**-space, obtained from the modulus of spatiotemporal Fourier transforms. Striking variations of the acoustic field penetration over the surface with frequency are evident in Fig. 3(a). At ~80 MHz, the acoustic wavelength is relatively long compared to the hole separation, and penetration is evident over the whole PC area. From the corresponding **k**-space image, which is dominated by the PC-region contribution, we estimate the wavelength to be ~24 μm with a corresponding sound velocity ~2000 ms^{-1}. We believe this frequency exhibits modes analogous to the antisymmetric A0 mode in an slab with no holes, as discussed in the Supplementary Information. The data at 161 MHz shows a similar behaviour, but with shorter wavelengths. At 241 and 322 MHz most of the acoustic energy is confined to the central cavity (as expected from the extent of the phononic band gap—see Section 3.2). At 402 MHz there is again efficient confinement. Approximate mode volumes V_m can be calculated [20,26] by integration up to the PC outer boundary using the equation $V_m = \int (|u_z|/\max|u_z|)^2\, h\, d^2\mathbf{r}$, where h is the slab thickness and u_z here represents a Fourier component, giving experimental values of 400 and 1400 μm^3 at 241 and 402 MHz, respectively. Modes outside the band gap, such as near 402 MHz, are "leaky", so their mode volume is formally infinite if the region of integration is extended to all space. Moreover, as we shall see below, these frequencies do not correspond exactly to "modes" since their frequencies are off resonance. However, the present estimations allow a rough comparison of the in-gap and outside-gap cases. At higher frequencies significant acoustic amplitude extends more than halfway to the PC outer boundary (see the Supplementary Information for constant-frequency animations).

The **k**-space plots of Fig. 3(b) are closely related to constant-frequency surfaces in the dispersion relation [42,44,45]. At 80 MHz, Bloch harmonics are clearly seen as faint rings surrounding the central bright ring. In addition to the Bloch harmonics, there is also a perturbative contribution from the effect of the spatially periodic optical reflectivity of the sample [45], which we shall ignore in this paper. At higher frequencies the Bloch harmonics produce more complex field patterns. Although the underlying silicon (111) slab has 3-fold rotational symmetry, the eigenmode field pattern is largely dominated by the 6-fold symmetric phononic lattice, except at 322 MHz where the experimental field pattern clearly shows evidence of 3-fold symmetry, visible in the real-space image in the central region. Such 3-fold symmetry has previously been noted in the vibrational field pattern of hexagonal pillars on (111) GaAs crystal surfaces [52], and is detectable in point-excited waves on a bare (111) slab (see the Supplementary Information). It is difficult to speculate on the reason why the 3-fold symmetry dominates only at certain frequencies.

3.2. Numerical simulations

To understand the experimental results we perform numerical acoustic simulations using PZFlex (Weidlinger Associates Inc.) and COMSOL Multiphysics (see the Supplementary Information). We first compare simulated dispersion relations for a slab with and without holes using literature values for the density and elastic constants. (Air damping is not expected to be significant [20]). For an identical silicon slab with no holes, and taking into account the anisotropy of the (111) cut, the dispersion relation calculated with COMSOL is shown in Fig. 4(a) for the [−2,1,1] propagation direction [see Fig. 1(a)]. The dispersion relation consists of Lamb modes, including antisymmetric (A), symmetric (S) and shear horizontal (SH) modes, of various orders. (See the Supplementary Information and below for further discussion of the slab without holes.) The SH modes do not engender out-of-plane motion. With the inclusion of holes, the PC lattice significantly modifies this relatively simple mode description. Figure 4(b) shows the frequency-domain COMSOL-simulated dispersion relation for a periodically repeated unit cell of the honeycomb-lattice PC silicon slab. A variety of modes are exhibited, as well as an omnidirectional band gap between 230 and 320 MHz.

Next, for direct comparison with experiment, we present time-domain simulations with PZFlex using a one-sided impulsive excitation (see the Supplementary Information for details, including the effect of ultrasonic attenuation ($\propto f^2$ [53]) and a simulation time window of 373 ns. This allows a higher spatial and frequency resolution (0.2 μm and 2.7 MHz) than is available in experiment (2 μm and 80 MHz), and gives access to the acoustic field over the whole 3D volume. The excitation is chosen to yield a similar phonon frequency spectrum ($\lesssim$1 GHz) to that observed in experiment, but rather than a periodic series of excitation pulses as in the experiment, we use a single pulse. (See the Supplementary Information for a time-domain 2D animation.)

Temporal and spatiotemporal Fourier transforms are shown in real- and **k**-space in Fig. 3(c) and (d), respectively, for the same frequencies as probed in experiment. The field patterns generally show very good agreement with experiment, including the rotational symmetry. Small differences could be caused by, apart from the different excitation, imperfections in the sample or by a small deviation of the pump spot from the central position. (Animations of these field patterns and those

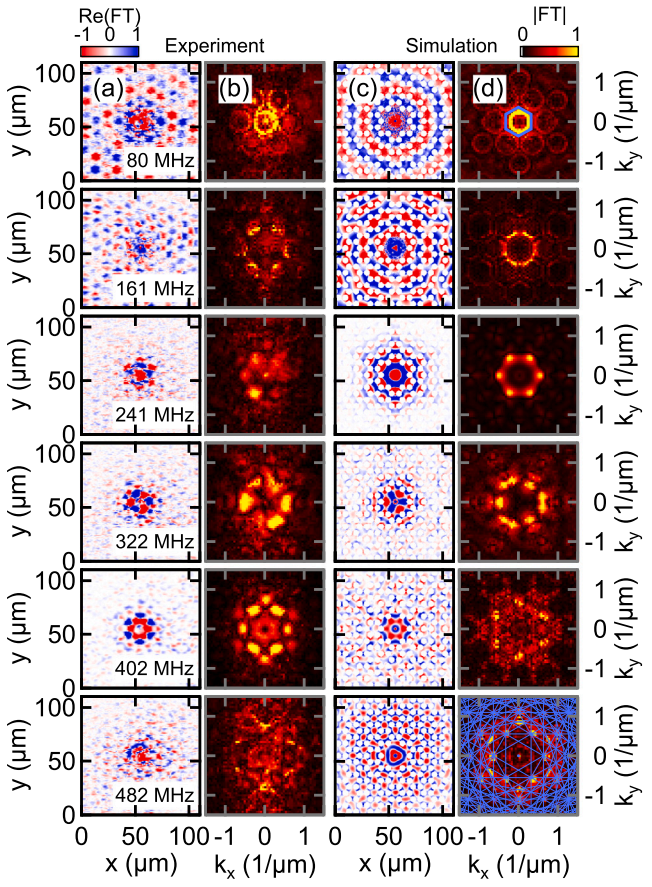

Fig. 3. Frequency-resolved acoustic fields. Experimental (a) real-space (temporal Re(FT)) and (b) **k**-space (spatiotemporal |FT|) fields compared with (c), (d) equivalent simulated fields. The first Brillouin Zone of the phononic lattice is indicated by the central hexagon (in blue) in (d) at 80 MHz. The complete BZ structure is shown in (d) at 482 MHz by the blue lines, and reciprocal lattice points are shown by the blue dots. The colour scales for each plot are normalized individually. FT: Fourier transform of the surface particle velocity u_z.

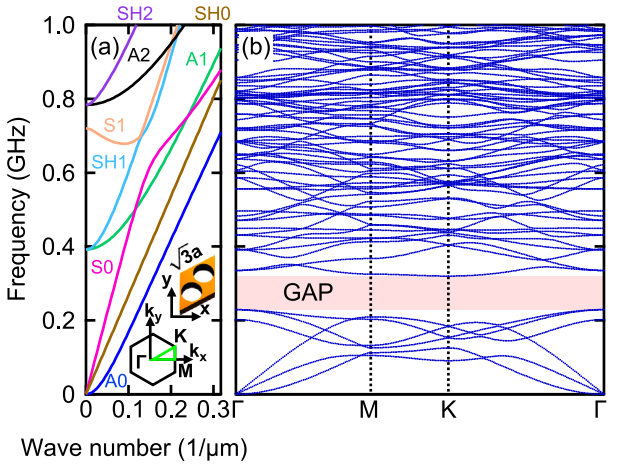

Fig. 4. Dispersion relation for laterally-propagating acoustic waves in a silicon (111) slab of thickness 6.5 μm for the [−2, 1, 1] (i.e. x) direction. (a) For a slab with no holes. Insets: unit cell and first Brillouin zone (BZ) for the honeycomb PC structure (hole spacing $a = 6.6$ μm). (b) For a similar slab with a honeycomb-lattice PC. The **k**-vector directions used in (b) correspond to the BZ inset in (a). A complete phononic band gap in the range 230 and 320 MHz is indicated by the pink shading. The horizontal scales measured in 1/μm are the same in (a) and (b).

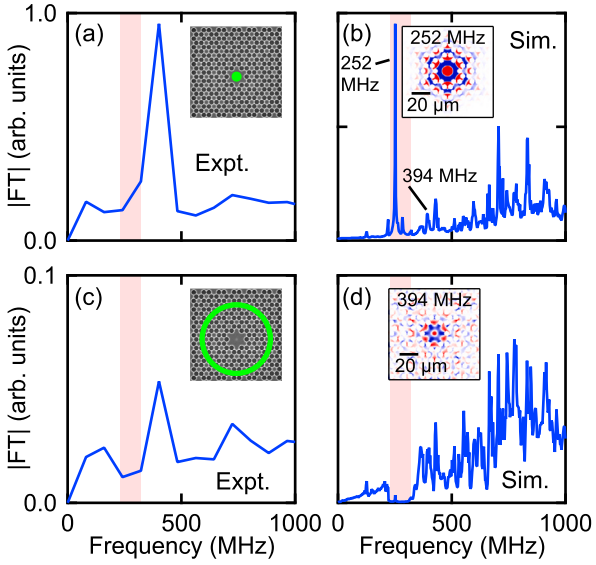

Fig. 5. Representative phononic spectra for experiment and simulation. (a) Experimental phonon spectrum in the cavity region. Inset: the (green) circle (of the same dimensions as that in Fig. 1) shows the region sampled. (b) Corresponding simulated phonon spectrum. Inset: mode field pattern at 252 MHz, plotted using Re(FT) as in Fig. 3. (c) Experimental phonon spectrum in an annular region away from the cavity. Inset: the (green) annulus shows the region sampled. (d) Simulated phonon spectrum in the annular region. The simulated band gap is indicated by the pink shading. Inset: mode field pattern at 394 MHz, plotted using Re(FT) as in Fig. 3. The vertical scales in the present figure can be compared to assess the relative amplitudes in the experiment or in the simulation. The colour scales of the insets are the same as in Fig. 3(c). Expt. and Sim. refer to experiment and simulation.

of the experiment are available in the Supplementary Information.) For the simulations at 80 MHz, the dominant phonon wavelength λ_x in the x direction is approximately equal to twice the honeycomb centre-to-centre distance, i.e. $\lambda_x = 2\sqrt{3}a \approx 23$ μm, or $k_x = \pi/(\sqrt{3}a) \approx 0.27\,\mu\text{m}^{-1}$, which is smaller than the corresponding value at the first Brillouin-zone (BZ) edge ($k_x = 2\pi/(3a) \approx 0.32\,\mu\text{m}^{-1}$). The BZ is shown by the blue hexagon in Fig. 3(d) in the 80 MHz image. At frequencies inside or near the calculated band gap, i.e. at 241 and 322 MHz respectively, the phonons are strongly attenuated outside the cavity, as observed in experiment. At higher frequencies, the field patterns in the simulations show significant penetration in the PC region. At 482 MHz, a striking real-space periodic field pattern is evident, leading to an array of bright dots in **k**-space, primarily at the zone centre and equivalent positions in translated BZs. At this frequency, the dispersion relation of Fig. 4(b) indicates that either a low-group velocity zone-centre eigenmode or ones at the 2nd BZ edge may be responsible. The effect of Bloch harmonics produces an array of dots in **k**-space at the centre of each translated BZ, as previously observed for other PC lattices [43,54]. We have superimposed the full BZ pattern on the image in Fig. 3(d) at 482 MHz using blue lines. Slab cross-section deformation plots, as well as a comparison between the PZFlex- and COMSOL-derived dispersion relations, are given in the Supplementary Information. The deformation plots allow one to determine if the predominant polarization at a specific frequency is symmetric or antisymmetric. The data of Fig. 3 all arise from prominently antisymmetric modes in the cavity region.

4. Discussion

4.1. Frequency spectra

Selective analysis of different regions of the sample surface allows a comparison between the phononic response inside the cavity with that outside. To analyse the cavity region, we average the modulus

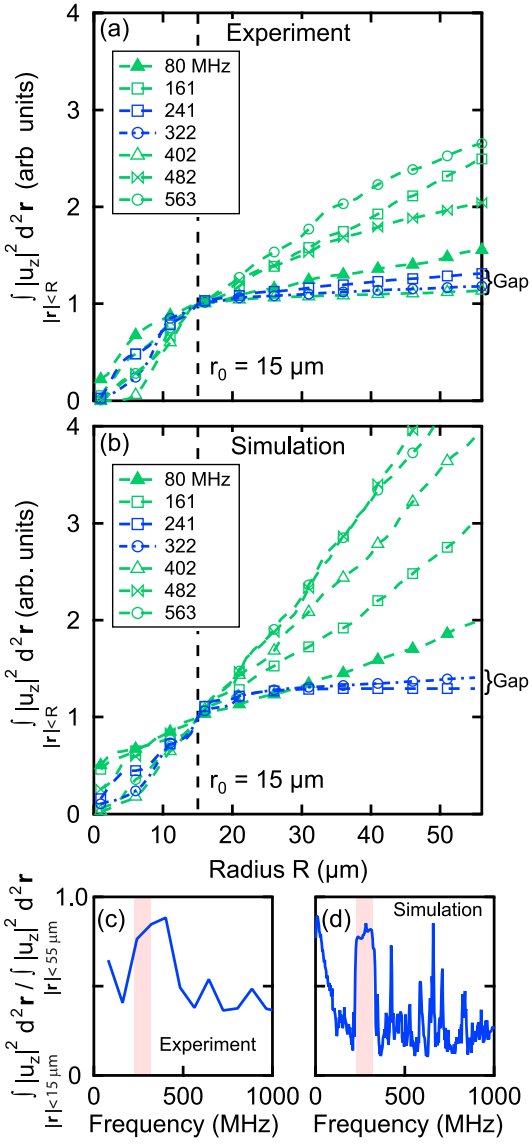

Fig. 6. Plots elucidating the radial dependence of the integral of $|u_z|^2$ in the cavity, correlated with the stored acoustic energy. Integrations are made over a region of radius R, where the cavity radius $r_0 = 15\,\mu m$ is shown in Fig. 1(a). (a) Experiment. (b) Simulation. The blue curves correspond to frequencies in or near the phononic band gap. (c), (d) Ratio of the integral of $|u_z|^2$ over a circle of radius $R = r_0$ to that over a circle of radius $R = 55\,\mu m$, for experiment and simulation, respectively. The simulated band gap is indicated by the pink shading. Vertical scales in (a) and (b) are normalized to a value of 1 at radius r_0. The calculations are done for each Fourier component individually.

of the temporal Fourier transform over an enclosing circle of radius 15 μm centred on the cavity, as indicated in Fig. 1(a). Phonon spectra obtained in this way are shown in Fig. 5(a) and (b) for experiment and simulation, respectively. For the experiment we observe a large peak at 402 MHz and a small one at 723 MHz. For the simulation we observe a large peak at 252 MHz and a number of smaller ones, for example at 394 and 705 MHz, close to those experimentally observed. One should not, however, expect an exact correspondence in the overall spectrum shapes in experiment and simulation owing to the ~80 MHz intervals accessed in experiment of a frequency spectrum with relatively fine peaks and the probable small differences in geometry between experiment and simulation. In addition, the simulations also have a finite frequency resolution (2.7 MHz), and may not accurately resolve narrow peaks. The simulated acoustic field patterns corresponding to the resonances at 252 and 394 MHz are shown in the insets of Fig. 5(b) and (d), respectively, both showing cavity confinement, as expected. These images show that although the experimentally probed frequencies at 241 and 402 MHz are off resonance, their acoustic field patterns appear to be dominated by the nearby resonant peaks.

Figure 5(c) and (d) show the modulus of the phonon spectrum averaged over an annulus of mean radius 47.5 μm (and thickness 5 μm), i.e., a distance ~7a from the centre (a = hole spacing), as indicated by the green ring in Fig. 5(c). The spectra of Fig. 5(c), (d) both show an expected dip around 230–320 MHz that spans the band gap, owing to the propagation through the PC region (over a radial distance ~5a).

The frequency of the in-gap 252 MHz peak in the simulation is expected to depend on the geometry of the cavity, which supports a variety of resonances. For reference we performed a simulation on a disc of radius 15 μm, with no holes, based on the identical slab thickness and crystal axes. The results (see the Supplementary Information) yield a similar radial dependence of the eigenmode fields. For the actual PC sample used, energy can leak out from the cavity into the surrounding PC lattice. However, the 252 MHz peak in the simulation falls inside the phononic band gap, so the observed strength of this peak can be attributed to efficient phonon confinement within the cavity at this frequency. Similar cavity resonances have previously been noted in PCs with defects [6,13,19–21]. This confinement is clear in Fig. 3 at 241 and 322 MHz for both experiment (a) and simulation (c). Comparison with the modes of the disc show that the two modes close to 241 and 402 MHz are analogous to those with radial mode numbers $n = 2$ and 3, respectively, in the isotropic case (see the Supplementary Information).

4.2. Quantitative analysis of the phononic confinement in the cavity

Cavity confinement can be quantified by monitoring the acoustic field as a function of the radial coordinate. Here we obtain a measure of this confinement related to the acoustic energy contained in a region consisting of a disc bounded by a circle of radius R by integrating $|u_z|^2$ up to R over the non-drilled area. Figure 6(a) and (b) show plots corresponding to experiment and simulation, respectively. The boundary of the cavity is provisionally defined as a circle of radius $r_0 = 15\,\mu m$ [see Fig. 1(a)]. (This radius approximately corresponds to the outside edge of the most centrally-placed holes.) The amplitude of the curves in these plots is each normalized relative to their amplitude at r_0, thereby removing the effect of the frequency dependence of the phonon excitation (see the Supplementary Information). The plots are indicative of the integrated acoustic energy density increasing with the size of the sampling circle. For a point-excited isotropic homogeneous sample at constant frequency, for radii sufficiently large compared to the wavelength λ, the in-plane acoustic field is expected to decay as $1/\sqrt{r}$ at radius r; a plot of acoustic energy within a radius R ($\propto \int (1/r)\, 2\pi r\, dr$) is therefore expected to be linear in R. (The inclusion of ultrasonic attenuation only produces a negligible decrease in the variation with R.) Although there are some differences between experiment and simulation, in both cases for the gap or near-gap frequencies 241 and 322 MHz there is a sharp kink at the cavity boundary accompanied by a change in slope, justifying the ad hoc choice of the cavity boundary and illustrating the role of the PC band gap. This sharp change is also observed at ~400 MHz in the experiment, but not in the simulation. This difference can be accounted for if one considers the small discrepancy in frequency between the high-Q resonance in the experiment and in the simulation. Some intermediate frequencies produce nearly linear curves in Fig. 6(a) and (b) (which would be expected from a homogenized theory of the effect of the PC lattice), although not at the lowest frequencies possibly because of the finite size of the PC region.

In order to quantify the confinement effect revealed in Fig. 6(a) and (b) in the frequency domain, we show in Fig. 6(c) and (d) the ratio of the total acoustic intensity in the cavity region ($r < 15\,\mu m$) to that in a circular region of radius 55 μm (~8a) for both experiment and

simulation, respectively, evaluated from the integral of $|u_z|^2$. A ratio of 1 would correspond to the case in which all the acoustic energy is contained within the cavity. The plots show clear peaks near the band gap in both cases, with a ratio of ~0.8 for frequencies inside the gap compared with ~0.4 outside, demonstrating the strikingly effective energy confinement within the band gap. The confinement can be further quantified by extracting the radial decay constant α of the field in the PC as a function of frequency in the region $25 < r < 55\,\mu m$, sufficiently removed from the cavity edge to avoid fields in the cavity interfering: $|FT(u_z)| \propto (1/\sqrt{r})\exp(-\alpha r)$, where FT denotes a temporal Fourier transform. As expected, the decay constant is much greater in the gap region: we extract $\alpha \approx 0.04\,\mu m^{-1}$ in experiment at 241 MHz (or $\alpha a \sim 0.25$), $\gtrsim$4 times the value outside the gap. The simulated value at this frequency, $\alpha \approx 0.1\,\mu m^{-1}$, may be higher because of the presence of homogeneities in the actual sample hole profile and owing to the sensitivity of the response at this frequency close to a resonance. (Details and plots are given in the Supplementary Information.)

4.3. Q factor of the main in-gap resonance

In this section we obtain by simulation the Q factor of the main in-gap eigenmode, of most practical interest because of the extreme acoustic confinement. The Q factor can be calculated as follows for the transient decay of a system at the resonant frequency f_0:

$$Q = \frac{2\pi f_0 E}{P}, \tag{1}$$

where $E = E_{kin} + E_{el}$ is the sum of the one-cycle-averaged kinetic and elastic strain energies integrated over the system volume and $P = P_{flux} + P_{atten}$ is the power loss from the PC system (i.e., the acoustic mode in question) owing to, respectively, the acoustic flux through the boundary enclosing the system and the rate of energy loss owing to ultrasonic attenuation at frequency f_0. Here we define the system to be a square of side 130 μm centred on the PC region. Even if the experimental frequency happened to tune precisely to a resonance, the acoustic field at the surface is not sufficient to determine the Q factor from Eq. (1). The simulations described previously do allow access to the full 3D acoustic field, but, in spite of the better frequency resolution, still lack that required to tune precisely to a resonance. However, the Q factor can be obtained from simulations by use of a cosine^2-envelope toneburst tuned to selectively excite an individual eigenmode, and allowing sufficient time for the system to stabilize afterwards. (We choose the envelope function $f(t) = (1 - \cos(2\pi t/T))^2$, where T is the total toneburst duration.) Eq. (1) can then be evaluated by calculation of E and P from the stress and strain tensor fields and from the acoustic Poynting vector. The power loss $P_{flux}\Delta t$ due to the acoustic energy flux P_{flux} through each plane element on the boundaries in one time step Δt is calculated from a knowledge of the energy flux in the $\pm x$ and $\pm y$ directions through the four planes perpendicular to the slab that bound the PC region, where

$$P_{flux} = \pm\Delta y\,\Delta z \sum_i \sum_j p_x^{ij} \pm \Delta x\,\Delta z \sum_i \sum_j p_y^{ij}, \tag{2}$$

and i and j represent indices to label plane elements of sides made up of two of the three lengths Δx, Δy, Δz on the respective surfaces. (The ± signs are chosen according to the element location—see the Supplementary Information) The p's are components of the Poynting vector given by $p_n = -\sigma_{nm}u_m$, where σ_{nm} is the stress tensor and u_n is the acoustic particle velocity vector. We calculate $E(t)$ using $E = E_{el} + E_{kin} = \frac{1}{2}\int(\sigma_{nm}\epsilon_{nm} + \rho\mathbf{u}^2)d^3\mathbf{r}$, where ϵ_{nm} is the strain tensor (see the Supplementary Information). This approach avoids the need for Fourier analysis, which is impractical owing to the relatively long mode lifetime (~100 ns). In contrast, by use of a toneburst one can selectively excite a single cavity mode and monitor its decay in the time domain using a simulation window much smaller than the mode decay time. Determining Q and the precise eigenmode frequency is possible provided that no modes are excited other than the one of interest.

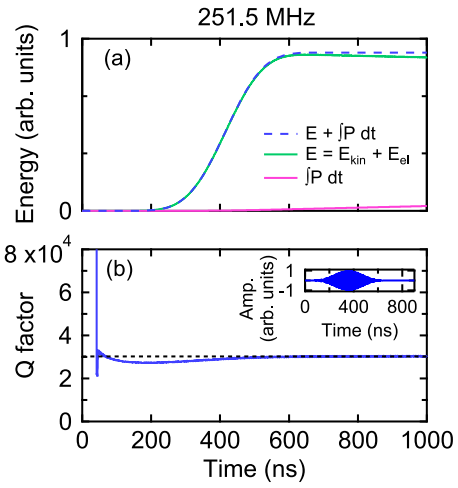

Fig. 7. Simulating energy loss processes and the Q factor. (a) Power-balance graph for the 251.5 MHz toneburst simulation in the presence of ultrasonic attenuation, showing the evolution of the stored energy in the system (green curve), the energy loss from the system (pink curve), and the sum of the elastic energy, the strain energy and the total integrated power loss (dashed blue curve). The energy loss includes both energy flux through the boundary and loss through ultrasonic attenuation. (b) Q factor vs time for the 251.5 MHz eigenmode as evaluated from Eq. (1). Inset: applied toneburst.

For the representative in-gap resonance that we previously identified at 252 MHz by the use of Fourier transforms, we find by an iterative series of simulations that 251.5 MHz corresponds more accurately to the eigenmode frequency closest to the corresponding in-gap simulated peak. Our cosine^2-envelope toneburst lasts for 180 periods, as shown in the inset of Fig. 7(a) (and described in detail in the Supplementary Information). Figure 7(a) shows plots of $\int P\,dt$, $E(t)$ and their sum calculated by simulation in the presence of ultrasonic attenuation, using a toneburst centred on 251.5 MHz. For energy conservation to be satisfied after the system stabilizes, E and $\int P\,dt$ should sum to a constant value at all times, which is indeed the case to an accuracy of ~1%. As previously mentioned, there are two sources of energy loss from the system that contribute to $P(t)$: acoustic flow through the system boundary and ultrasonic attenuation losses. Figure 7(b) shows a plot of the corresponding Q factor vs time obtained by use of Eq. (1). The convergence of this curve to a fixed value demonstrates that the system starts to stabilize after the toneburst finishes, at which point the energy in the vibrational response of the system is closely attributable to a single eigenmode, allowing the extraction of a unique Q factor.

At 251.5 MHz we find $Q = (2.98 \pm 0.05) \times 10^4$. The corresponding full peak width at half maximum (FWHM) value in intensity is Δf~0.01 MHz. It is remarkable that to reliably determine the shape of this resonance peak to find Q by a temporal Fourier transform, one would need a time interval of at least $\sim Q/f_0 \sim 80\,\mu s$, whereas here by means of a quasi-monotone toneburst to excite only the single eigenmode of interest, we achieve the same in ~0.5 μs. Not only is the saving in computation time huge, but in practice it would not be easy to eliminate numerical errors to obtain high Q factors $\gtrsim 10^4$ using the Fourier transform method.

Our in-gap result for Q at 251.5 MHz is consistent with previous experimental results obtained for 2D PCs up to GHz frequencies at room temperature. Published values at such temperatures include 6.3×10^3 for a 2D PC slab at ~130 MHz [6], 2×10^4 for a 2D PC slab at ~5 MHz [19], and 4.2×10^3 for a quasi 1D PC in a 2D PC slab at ~0.5 GHz [20]. Higher values, e.g. 4.9×10^{10} for a GHz nanoacoustic resonator [33], are obtainable at ultra-low temperatures where ultrasonic attenuation is greatly diminished.

In order to assess the influence of ultrasonic attenuation on the Q factor, we further conducted simulations without attenuation (see the Supplementary Information): we obtain $Q = (4.9 \pm 0.3) \times 10^5$ at

251.5 MHz. This in-gap value of Q, ~16 times that for the attenuated system, shows that for the fabricated PC structure the in-gap-resonance Q factor is primarily limited by energy loss through ultrasonic attenuation. Clearly one could obtain arbitrarily higher values of Q in the absence of attenuation by increasing the size of the PC region around the cavity. In practice, to increase Q it would suffice to cool the sample to lower the ultrasonic attenuation.

5. Conclusions

In conclusion, we experimentally image the acoustic field in a 2D phononic-crystal cavity over a broad range of frequencies up to ~1 GHz by means of a time-resolved optical pump-probe technique. We analyse our results in real space in both the time and frequency domains as well as in **k**-space. Comparison with finite-element simulations using impulsive excitation confirms the presence of a wide phononic band gap between 230 and 320 MHz, in agreement with the simulated dispersion relation. The acoustic fields at 241 and 322 MHz measured in the vicinity of this band gap exhibit strong localization in the cavity. The simulations also reveal a pronounced resonance at ~252 MHz, lying inside the band gap, arising from the trapping of acoustic energy within the cavity region in a quasi $n = 2$ mode, where n is the radial mode number of an isotropic disc of similar diameter. Other simulated resonances include one at ~400 MHz in a quasi $n = 3$ mode, which we assume to be associated with the dominant response observed experimentally because of the coincidental proximity of this resonance to an integral multiple of the laser repetition frequency. Radial plots of the acoustic intensity show a pronounced kink at the cavity boundary at the above experimental frequencies for strong localization, and phonon spectra extracted at the centre of the cavity and near the edge of the PC region further demonstrate the prominent role of the band gap in the spatial decay, which is quantitatively derived as an attenuation constant. The Q factor of the inside-gap ~252 MHz resonance peak is found by simulation using a method involving toneburst excitation to be $Q \sim 30000$, limited primarily by ultrasonic attenuation.

This work thus establishes wideband phonon imaging and its comparison to simulations as an important tool in quantifying the acoustic eigenstate 2D spatial extent and energy localization in 2D PC cavities. Our approaches in both experiment and simulation, crucially involving omnidirectional phonon propagation, should be applicable to a variety of such cavities, and help reveal the factors contributing to their ability to store acoustic energy. Applications are expected in elucidating the response of surface-phonon based sensors and filters [13,55], and potentially in vibrational energy harvesting [7,14,23]. Moreover, the imaging of PC cavities should provide informative feedback to the photonic case, and lead to joint optical and acoustic imaging studies where phonons and photons are simultaneously confined in 2D on microscopic scales [30,56,57].

Declaration of competing interest

The authors declare that they have no known competing financial interests or personal relationships that could have appeared to influence the work reported in this paper.

Data availability

Data will be made available on request

Acknowledgements

We acknowledge Grants-in-Aid for Scientific Research from the Ministry of Education, Culture, Sports, Science and Technology (MEXT) as well as support from the Japanese Society for the Promotion of Science (JSPS). The contribution by A.A.M was supported by the Department of Energy, Office of Science, Office of Basic Energy Sciences, under Award Number DE-SC0019126.

Appendix A. Supplementary data

Supplementary material related to this article can be found online at https://doi.org/10.1016/j.pacs.2023.100481.

References

[1] M. Torres, F.R. Montero de Espinosa, D. García-Pablos, N. García, Sonic band gaps in finite elastic media: Surface states and localization phenomena in linear and point defects, Phys. Rev. Lett. 82 (15) (1999) 3054–3057.
[2] A. Khelif, et al., Trapping and guiding of acoustic waves by defect modes in a full-band-gap ultrasonic crystal, Phys. Rev. B 68 (21) (2003) 214301.
[3] A. Khelif, A. Choujaa, S. Benchabane, B. Djafari-Rouhani, V. Laude, Guiding and bending of acoustic waves in highly confined phononic crystal waveguides, Appl. Phys. Lett. 84 (22) (2004) 4400.
[4] F.-L. Hsiao, et al., Waveguiding inside the complete band gap of a phononic crystal slab, Phys. Rev. E 76 (5) (2007).
[5] L.-Y. Wu, L.-W. Chen, C.-M. Liu, Acoustic pressure in cavity of variously sized two-dimensional sonic crystals with various filling fractions, Phys. Lett. A 373 (12) (2009) 1189–1195.
[6] S. Mohammadi, A.A. Eftekhar, W.D. Hunt, A. Adibi, High-Q micromechanical resonators in a two-dimensional phononic crystal slab, Appl. Phys. Lett. 94 (5) (2009) 051906.
[7] L.-Y. Wu, L.-W. Chen, C.-M. Liu, Acoustic energy harvesting using resonant cavity of a sonic crystal, Appl. Phys. Lett. 95 (1) (2009) 013506.
[8] V. Romero-García, J.V. Sánchez-Pérez, L.M. Garcia-Raffi, Propagating and evanescent properties of double-point defects in sonic crystals, New J. Phys. 12 (8) (2010) 083024.
[9] M. Ziaei-Moayyed, M.F. Su, C.M. Reinke, I. El-Kady, R.H. Olsson, Silicon carbide phononic crystals for high f.Q micromechanical resonators, in: 2010 IEEE International Ultrasonics Symposium, 2010, pp. 162–166.
[10] N. Wang, et al., Experimental investigation of a cavity-mode resonator using a micromachined two-dimensional silicon phononic crystal in a square lattice, IEEE Electron Device Lett. 32 (6) (2011) 821–823.
[11] F. Li, J. Liu, Y. Wu, The investigation of point defect modes of phononic crystal for high Q resonance, J. Appl. Phys. 109 (12) (2011) 124907.
[12] R. Marchal, et al., Dynamics of confined cavity modes in a phononic crystal slab investigated by *in situ* time-resolved experiments, Phys. Rev. B 86 (22) (2012) 224302.
[13] R. Lucklum, M. Ke, M. Zubtsov, Two-dimensional phononic crystal sensor based on a cavity mode, Sensors Actuators B 171–172 (2012) 271–277.
[14] H. Lv, X. Tian, M.Y. Wang, D. Li, Vibration energy harvesting using a phononic crystal with point defect states, Appl. Phys. Lett. 102 (3) (2013) 034103.
[15] N. Wang, F.-L. Hsiao, M. Palaniapan, C. Lee, Evidence on simultaneous improvement of motional impedance and Q-factor of silicon phononic crystal micromechanical resonators by variously engineering the cavity defects, J. Appl. Phys. 115 (9) (2014) 094904.
[16] P. Celli, S. Gonella, Manipulating waves with LEGO® bricks: A versatile experimental platform for metamaterial architectures, Appl. Phys. Lett. 107 (8) (2015) 081901.
[17] M. Ghasemi Baboly, S. Alaie, C.M. Reinke, I. El-Kady, Z.C. Leseman, Ultra-high frequency, high Q/volume micromechanical resonators in a planar AlN phononic crystal, J. Appl. Phys. 120 (3) (2016) 034502.
[18] D. Goettler, et al., Realizing the frequency quality factor product limit in silicon via compact phononic crystal resonators, J. Appl. Phys. 108 (8) (2010) 084505.
[19] P. Li, et al., Temperature insensitive mass sensing of mode selected phononic crystal cavity, J. Micromech. Microeng. 25 (12) (2015) 125027.
[20] D. Hatanaka, H. Yamaguchi, Real-space characterization of cavity-coupled waveguide systems in hypersonic phononic crystals, Phys. Rev. A 13 (2) (2020) 024005.
[21] X. Li, Z. Liu, Coupling of cavity modes and guiding modes in two-dimensional phononic crystals, Solid State Commun. 133 (6) (2005) 397–402.
[22] F.-C. Hsu, T.-T. Wu, J.-C. Hsu, J.-H. Sun, Directional enhanced acoustic radiation caused by a point cavity in a finite-size two-dimensional phononic crystal, Appl. Phys. Lett. 93 (20) (2008) 201904.
[23] S. Qi, M. Oudich, Y. Li, B. Assouar, Acoustic energy harvesting based on a planar acoustic metamaterial, Appl. Phys. Lett. 108 (26) (2016) 263501.
[24] C.T. Nguyen, MEMS technology for timing and frequency control, IEEE Trans. Ultrason. Ferroelectr. Freq. Control 54 (2) (2007) 251–270.
[25] P. Lalanne, C. Sauvan, J. Hugonin, Photon confinement in photonic crystal nanocavities, Laser Photonics Rev. 2 (6) (2008) 514–526.
[26] R. Coccioli, M. Boroditsky, K. Kim, Y. Rahmat-Samii, E. Yablonovitch, Smallest possible electromagnetic mode volume in a dielectric cavity, IEE Proc. 145 (6) (1998) 391–397.
[27] C. Reese, et al., High-q photonic crystal microcavities fabricated in a thin GaAs membrane, J. Vac. Sci. Technol. B 19 (6) (2001) 2749–2752.
[28] H.-Y. Ryu, M. Notomi, G.-H. Kim, Y.-H. Lee, High quality-factor whispering-gallery mode in the photonic crystal hexagonal disk cavity, Opt. Express 12 (8) (2004) 1708–1719.

[29] K.J. Vahala, Optical microcavities, Nature 424 (6950) (2003) 839–846.
[30] M. Maldovan, E. Thomas, Simultaneous complete elastic and electromagnetic band gaps in periodic structures, Appl. Phys. B 83 (4) (2006) 595–600.
[31] A. Fainstein, N.D. Lanzillotti-Kimura, B. Jusserand, B. Perrin, Strong optical-mechanical coupling in a vertical GaAs/AlAs microcavity for subterahertz phonons and near-infrared light, Phys. Rev. Lett. 110 (3) (2013) 037403.
[32] S. Anguiano, et al., Micropillar resonators for optomechanics in the extremely high 19–95-GHz frequency range, Phys. Rev. Lett. 118 (26) (2017) 263901.
[33] G.S. MacCabe, et al., Nano-acoustic resonator with ultralong phonon lifetime, Science 370 (6518) (2020) 840–843.
[34] X. Zhang, T. Jackson, E. Lafond, P. Deymier, J. Vasseur, Evidence of surface acoustic wave band gaps in the phononic crystals created on thin plates, Appl. Phys. Lett. 88 (4) (2006) 041911.
[35] J.O. Vasseur, P.A. Deymier, B. Djafari-Rouhani, Y. Pennec, A.-C. Hladky-Hennion, Absolute forbidden bands and waveguiding in two-dimensional phononic crystal plates, Phys. Rev. B 77 (8) (2008) 085415.
[36] T.-T. Wu, Z.-G. Huang, T.-C. Tsai, T.-C. Wu, Evidence of complete band gap and resonances in a plate with periodic stubbed surface, Appl. Phys. Lett. 93 (11) (2008) 111902.
[37] K. Yu, T. Chen, X. Wang, A. Zhou, Large band gaps in phononic crystal slabs with rectangular cylinder inclusions parallel to the slab surfaces, J. Phys. Chem. Solids 74 (8) (2013) 1146–1151.
[38] D. Feng, W. Jiang, D. Xu, B. Xiong, Y. Wang, Acoustic wave characterization of silicon phononic crystal plate, Appl. Phys. Lett. 107 (9) (2015) 091907.
[39] F. Shu, Y. Liu, J. Wu, Y. Wu, Band gap in tubular pillar phononic crystal plate, Ultrasonics 71 (2016) 172–176.
[40] Y. Jin, Y. Pennec, Y. Pan, B. Djafari-Rouhani, Phononic crystal plate with hollow pillars actively controlled by fluid filling, Crystals 6 (6) (2016) 64.
[41] Y. Jin, et al., Tunable waveguide and cavity in a phononic crystal plate by controlling whispering-gallery modes in hollow pillars, Phys. Rev. B 93 (5) (2016) 054109.
[42] D. Profunser, O. Wright, O. Matsuda, Imaging ripples on phononic crystals reveals acoustic band structure and Bloch harmonics, Phys. Rev. Lett. 97 (5) (2006).
[43] D.M. Profunser, E. Muramoto, O. Matsuda, O.B. Wright, U. Lang, Dynamic visualization of surface acoustic waves on a two-dimensional phononic crystal, Phys. Rev. B 80 (1) (2009) 014301.
[44] P.H. Otsuka, et al., Broadband evolution of phononic-crystal-waveguide Eigenstates in real- and k-spaces, Sci. Rep. 3 (2013) 3351.
[45] P.H. Otsuka, et al., Effect of excitation point on surface phonon fields in phononic crystals in real- and k-space, J. Appl. Phys. 117 (24) (2015) 245308.
[46] Q. Xie, et al., Imaging gigahertz zero-group-velocity lamb waves, Nature Commun. 10 (1) (2019) 1–7.
[47] S. Kim, J. Lee, H. Jeon, H.J. Kim, Fiber-coupled surface-emitting photonic crystal band edge laser for biochemical sensor applications, Appl. Phys. Lett. 94 (13) (2009) 133503.
[48] S. Mohammadi, et al., Complete phononic bandgaps and bandgap maps in two-dimensional silicon phononic crystal plates, Electron. Lett. 43 (16) (2007) 898–899.
[49] S. Mohammadi, A.A. Eftekhar, A. Khelif, W.D. Hunt, A. Adibi, Evidence of large high frequency complete phononic band gaps in silicon phononic crystal plates, Appl. Phys. Lett. 92 (22) (2008) 221905.
[50] T. Tachizaki, et al., Scanning ultrafast Sagnac interferometry for imaging two-dimensional surface wave propagation, Rev. Sci. Instrum. 77 (4) (2006) 043713.
[51] M. Nomura, et al., Impeded thermal transport in Si multiscale hierarchical architectures with phononic crystal nanostructures, Phys. Rev. B 91 (20) (2015) 205422.
[52] H. Sakuma, et al., Vibrational modes of GaAs hexagonal nanopillar arrays studied with ultrashort optical pulses, Appl. Phys. Lett. 100 (13) (2012) 131902.
[53] D. Li, D.G. Cahill, Attenuation of 7 GHz surface acoustic waves on silicon, Phys. Rev. B 94 (10) (2016) 104306.
[54] O. Matsuda, et al., Refraction, beam splitting and dispersion of GHz surface acoustic waves by a phononic crystal, Photoacoustics 30 (2023) 100471.
[55] K. Länge, B.E. Rapp, M. Rapp, Surface acoustic wave biosensors: a review, Anal. Bioanal. Chem. 391 (5) (2008) 1509–1519.
[56] Q. Rolland, et al., Acousto-optic couplings in two-dimensional phoxonic crystal cavities, Appl. Phys. Lett. 101 (6) (2012) 061109.
[57] R. Lucklum, M. Zubtsov, A. Oseev, Phoxonic crystals—a new platform for chemical and biochemical sensors, Anal. Bioanal. Chem. 405 (20) (2013) 6497–6509.

Paul Otsuka obtained his Ph.D. in Physics from The University of Melbourne in Australia in 2005, and currently works at the Faculty of Engineering at Hokkaido University in Japan. His research interests include laser ultrasonics, acoustic imaging, phononic crystals, and acoustic metamaterials.

Ryota Chinbe received his B.A. degree in Engineering in 2011 and his master's degree in 2013 from Hokkaido University, Sapporo, Hokkaido, Japan. His research interests include laser picosecond ultrasonics and surface acoustic wave imaging.

Motonobu Tomoda received his Ph.D. degree in Engineering at Hokkaido University, Sapporo, Hokkaido, Japan, in 2008. Since 2022, he has been working as an Instructor (until 2007) and an Assistant Professor (from 2007) in the Faculty of Engineering, Hokkaido University. He specializes in picosecond laser ultrasonics in nanostructures, local probing techniques involving ultrasonics and optics, surface acoustic wave imaging, phononic crystals, and acoustic/mechanical metamaterials.

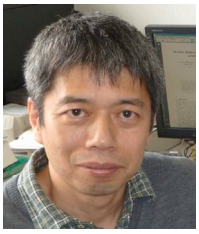

Osamu Matsuda received his Ph.D. degree in Physics at Osaka University, Japan in 1991. He is currently a Professor at Hokkaido University, Japan. His research interests include ultrafast spectroscopy, picosecond laser ultrasonics, acoustic wave imaging, phononic crystals, and phononic metamaterials.

Yukihiro Tanaka received his Ph.D. degree in Engineering at Hokkaido University, Sapporo, Hokkaido, Japan, in 1997. He is currently a Professor at Hokkaido University of Education, Asahikawa, Hokkaido, Japan. He specializes in ultrasonic waves and phonons in nanostructures, phononic crystals, and acoustic/mechanical metamaterials.

Dieter M. Profunser After his Ph.D. on picosecond ultrasonics at the Swiss Federal Institute of Technology in Zurich (Switzerland), in 2004 Dieter M. Profunser joined the Applied Solid State Physics lab of Oliver B. Wright at Hokkaido University (Japan). His focus was high frequency imaging in phononic crystal structures. From 2007, he holds different R&D roles in an international corporation.

Sihan Kim studied Physics at Seoul National University, graduating with B.A. and Ph.D. degrees in 2005 and 2012, respectively. He currently holds a position at Samsung Electronics, developing microLED technologies.

Heonsu Jeon has been a Professor at Seoul National University, Korea, since 1998. He received his B.A. and M.S. in Physics at Seoul National University and his Ph.D. in Physics from Brown University, USA. His current research interests include the fundamentals and applications of photonic crystals, nanophotonics, and topological photonics.

Istvan A. Veres has been a Member of Technical Staff at Qorvo, USA since 2017. He received his MSc in Structural Engineering at the Technical University of Budapest and his PhD from the ETH Zurich. In his current position he investigates piezoelectric resonators and piezoelectric materials.

Alex Maznev received a Diploma in Physics from the Moscow Institute of Physics and Technology and a Ph.D. from the General Physics Institute of the Russian Academy of Sciences (thesis on laser-generated surface acoustic waves including the first observation of surface phonon focusing). He held postdoctoral positions at the Freie Universität Berlin, as a Humboldt Fellow, and at MIT, where he developed an optical heterodyning scheme for laser-induced transient grating experiments currently used in many labs. Subsequently, he worked as an industrial researcher developing photoacoustic metrology systems for the semiconductor industry, before returning to MIT as a Staff Scientist. His current interests involve a range of topics pertaining to wave propagation phenomena, primarily in acoustics and related fields such as phonon-mediated heat transport on the micro/nanoscale.

Oliver B. Wright has been a Professor at Hokkaido University, Japan since 1996 and a Guest Professor at Osaka University, Japan since 2022. He received his B.A. in Physics at the University of Oxford and his Ph.D. in Physics from the University of Cambridge. His current research interests include picosecond laser ultrasonics, acoustic wave imaging, and acoustic metamaterials.